Band Alignment and Optical Properties of 1D/2D Sb2Se3/PtSe2 Heterojunctions

Kapil Bhorkar, Labrini Sygellou, Michel Cathelinaud, Donglou Ren, Jean-Luc Adam, Spyros N. Yannopoulos

Band alignment and optical properties of 1D/2D $Sb_2Se_3/PtSe_2$ heterojunctions

Kapil Bhorkar,[a,b,*,] Labrini Sygellou,[a] Michel Cathelinaud,[b] Donglou Ren[b], Jean-Luc Adam,[b] and Spyros N. Yannopoulos [a,*]

[a] *Foundation for Research and Technology Hellas – Institute of Chemical Engineering Sciences (FORTH/ICE-HT), P.O. Box 1414, GR-26504, Rio-Patras, Greece*

[b] *Univ Rennes, CNRS, ISCR - UMR 6226, F-35000 Rennes, France*

*Corresponding authors: sny@iceht.forth.gr, kapilbhorkar@gmail.com

Abstract

The heterojunction between two materials brought into contact, for example in the form of vertical van der Waals heterostructures, exhibit interesting features offering functionalities to devices stimulated by light. We report in this article, an investigation of the optical and electronic properties of the heterojunction formed between Sb_2Se_3, a material with promising role in photovoltaics characterized by 1D topology (ribbons) and an emerging 2D material, $PtSe_2$, exhibiting unique optical properties for photoelectronics and photonics. The controlled growth of $PtSe_2$ on Sb_2Se_3 underlayer takes place using a transfer-free process by low temperature selenization of 1-2 nm Pt films thermally evaporated on Sb_2Se_3 ultrathin substrates. XPS data analyzed in the context of the Kraut method, provided an estimate for the band offsets at the interface. The valence band offset and the conduction band offset of the $PtSe_2/Sb_2Se_3$ heterojunction was found to be $-0.25eV$ and$1.0eV$, respectively, indicating a type-II heterojunction. The ultrabroad optical absorption of the heterojunction and the protection offered by $PtSe_2$ to Sb_2Se_3, against oxidation of the latter, render this particular heterojunction a robust candidate for applications in photovoltaics. Finally, the current study of a heterojunction between materials of different dimensionality, may pave the way for a rational design in the field of trans-dimensional heterostructures.

Keywords: $PtSe_2$, Sb_2Se_3, type-II heterostructure, band alignment, self-powered photodetector, thermally assisted conversion (TAC)

1. Introduction

A great deal of effort has been dedicated over the last years to understand basic phenomena and application-oriented subtleties for a very large number of two-dimensional (2D) crystals. Apart from discovering unconceivable new physics, the exploration of 2D materials has paved the way for a wide range of potential applications related to energy, environment, bioscience, and high-technology products [1]. Graphene-related materials and group VIB transition metal dichalcogenides (TMDCs) have dominated, during the past years, fundamental studies and device evaluation. Vertical and horizontal heterojunctions of various types of 2D crystals, have also emerged as promising combinations of materials, which offer additional functional features at the heterojunction, by combining the unique properties of the individual crystals [2]. Besides enhanced performance, simple fabrication processes of heterojunction devices is of vital importance for up-scaling and production compatibility. Here, we demonstrate, for the first time, the scalable low temperature growth of heterojunctions based of 1D-Sb_2Se_3 and 2D-$PtSe_2$. Investigations of their optical properties and band alignment, highlight the prospects of this heterojunction in optoelectronic devices such as excitonic transistors, switches, lasers and photo-detectors [3].

Antimony triselenide, which belongs to group 6 chalcogenides, differs from TMDCs as it is considered a one-dimensional (1D) semiconducting crystal composed of $(Sb_4Se_6)_n$ ribbons arranged along the (001) direction. The ribbons are covalently bonded, interacting via weak van der Waals forces forming two-dimensional layers. Antimony chalcogenides have been mostly known as non-crystalline materials prepared as amorphous films and/or glasses [4]. Bulk glasses can be prepared at any composition of the binary Sb_xSe_{40-x} system for the composition range $0 \leq x \leq 30$ [5]. Due to its low optical bandgap and large absorption coefficient, the stoichiometric compound, Sb_2Se_3, has

attracted vivid attention over the last years as absorbing material for potential applications in photovoltaics [6,7].

The layered structure of group-10 or noble-transition metal dichalcogenides, such as $PtSe_2$, is known since decades [8,9]. However, the development of novel experimental methods and theoretical tools for 2D materials, have brought group-10 dichalcogenides again under focus [10–12]. Few-layer $PtSe_2$ crystals exhibit fascinating photonic and optoelectronic properties [13]. High-quality $PtSe_2$ crystals of controlled thickness can be produced in a variety of ways compatible with current technology platforms. A major merit of $PtSe_2$ is that it can be grown at much lower temperatures, i.e. below 450 ^oC, in contrast to other TMDCs. This enables the $PtSe_2$ growth on temperature-sensitive underlayers, such as Sb_2Se_3. While bulk or multi-layer $PtSe_2$ exhibit semimetallic character (zero bandgap) the monolayer exhibits semiconducting properties ($E_g \approx 1.2$ eV). The layer-dependent broad distribution of the bandgap energy straddles up the mid-IR region, rendering few-layer $PtSe_2$ an essential photonic material. While systematic studies have been undertaken for few-layer $PtSe_2$ pristine crystals, investigations concerning properties of van der Waals heterojunctions based on $PtSe_2$ with other 2D crystals are still sporadic in the literature.

Because Sb_2Se_3 and $PtSe_2$ have emerged as two very important optical materials we attempt here an exploration of the optical and electronic properties for the vertical heterojunction formed by these two crystals. It is well-known that Sb_2Se_3 is highly prone to oxidation which could alter its properties and hence its performance as a solar absorbing layer in photovoltaics. Hence, studies have focused on investigating the band alignment details between Sb_2O_3 and Sb_2Se_3 [14]. The increased interest on Sb_2Se_3-based heterojunctions is demonstrated by recent studies exploring combinations with ZnO for self-powered, flexible photodetectors [15] and self-powered broad spectral photodetectors

with fast response based on Sb_2Se_3/VO_2 heterojunctions [16]. Owing to the very high stability of $PtSe_2$ at environmental conditions, $PtSe_2$ / Sb_2Se_3 heterojunctions could emaciate the propensity of Sb_2Se_3 to oxidation by providing a protective layer, which at the same time increases the light absorbance towards the mid-infrared.

2. Experiments

2.1 Materials preparation

Sb_2Se_3 films with various thicknesses (< 5 nm, 150, and 320 nm) were deposited on BK7 glass substrates; hereafter, films with thickness < 5 nm will be denoted as ultrathin films. Before deposition, substrates were ultrasonically cleaned using detergent, ethanol and deionized water for 10 min. Sb_2Se_3 amorphous films were deposited onto substrates by RF magnetron sputtering with a 99.99% pure stoichiometric Sb_2Se_3 target obtained by high temperature melting method [17]. The pressure of the vacuum chamber was less than 3×10^{-5} Pa before deposition. The Sb_2Se_3 target was initially etched by argon plasma for about 10 min to eliminate surface contaminants. The working pressure and sputtering power were fixed at 0.5 Pa and 12 W, respectively with 30 sccm of Ar, to obtain a low and constant deposition rate. The substrate temperature was not specifically controlled during the sputtering process. The amorphous as-deposited films were crystallized by heating at 300 °C for 60 minutes, under a pressure of 0.2 mbar [18]. The sputtering times were 1, 36 and 80 min, which correspond to film thicknesses of < 5 nm, 150, and 320 nm, respectively. The 150 and 320 nm films thicknesses were determined by spectrophotometer method [19]. The 1 min sputtered ultrathin film was estimated to be ~3 nm in thickness.

$PtSe_2$ / Sb_2Se_3 heterojunctions were grown by depositing ultrathin layers of Pt (between 1-2 nm nominal thickness) on top of the ultrathin Sb_2Se_3 surface by thermal

evaporation, followed by low temperature selenization using pellets of ultrapure Se (Alfa Aesar, purity 99.9990%). The selenization step took place in a tube furnace at 430 ^{o}C for 90 min, under the flow of N_2/H_2:95/5 gas at a flow rate of 100 sccm. Pristine $PtSe_2$ films were also prepared on Si/SiO_2 and SiO_2 substrates, following the same procedure, to study their properties in relation to the heterojunctions. Direct growth of $PtSe_2$ on Sb_2Se_3 avoids any transfer step of the heterojunctions, as has been the case in previous studies, hence preventing contamination and alteration of the as-grown heterojunctions.

2.2 Materials characterization

Raman spectra were recorded at room temperature using the micro-Raman Jobin-Yvon (T-64000) spectrometer and 1800 grooves/mm gratings for the analysis. Spectra were excited with a He-Ne laser (632.8 nm or 1.96 eV) using a power less than 0.2 mW on the sample. This intensity is low enough to secure that thermal-induced oxidation of Sb_2Se_3 films is avoided, within the time scale of spectra accumulation. A large number of spectra were collected from various points of the films surface to ensure homogeneity of the grown materials. The absorption spectra were recorded with a Perkin–Elmer (model Lambda 900) spectrophotometer over a broad spectral range (2800 to 350 nm). Optical spectra were also recorded repetitively from various areas of the samples, demonstrating identical spectra shapes. Electron microscopy images for characterizing the surface morphology of the heterostructure, were recorded by a high-resolution field-emission scanning electron microscope (FE-SEM) instrument (Zeiss, SUPRA 35VP) operating at 10 kV.

X-ray and ultra-violet photoelectron spectroscopies (XPS and UPS) were performed in UHV ($P\sim5\times10^{-10}$ mbar) system equipped with a hemispherical electron analyzer

(SPECS, Phoibos 100-1D-DLD) and a non-monochromatized dual-anode Mg/Al x-ray gun. The spectra were recorded with MgKa at 1253.6 eV photon energy and an analyzer pass energy of 10 eV giving a Full Width at Half Maximum (FWHM) of 0.85 eV for Ag3d5/2 line. The analyzed area corresponds to a spot of ~3 mm diameter. For spectra collection and treatment, including fitting, the commercial software SpecsLab Prodigy (by Specs GmbH, Berlin) was used. The XPS peaks were fitted by decomposing each spectrum into individual mixed Gaussian-Lorentzian peaks after a Shirley background subtraction. The atomic ratios were calculated from the intensity of the XPS peaks divided by the appropriate relative sensitivity factors derived from the Scofield cross-section taking into account the electron transport properties of the matrix, and the energy analyzer transmission function characteristics. For UPS measurements a UV source (model UVS 10/35) was employed, using HeI irradiation (hν=21.22 eV) with the analyzer operating at the Constant Retarding Ratio (CRR) mode, with CRR=3. The work function (WF) and the Valence Band Maximum cut off (VBM) were directly estimated by the UPS spectra, by linear extrapolation of the high and low energy cutoffs to the baseline and determining their intersections with the binding energy axis. For the WF determination a bias of −12.30 V was applied to the sample to avoid interference of the spectrometer threshold in the UPS spectra.

3. Results and Discussion

FE-SEM images at different magnifications are show in Fig. S1, demonstrating the surface morphology of the as prepared heterostructure, which reveals their polycrystalline nature. This morphology is expected as the top layer, $PtSe_2$, is synthesized by selenizing the pre-deposited Pt films. The morphology is identical to that of previously reported $PtSe_2$ films grown using thermally assisted conversion (TAC) method [20,21]. The thickness of the Sb_2Se_3 layer has been estimated by atomic

force microscopy (AFM). A typical AFM image and the corresponding height profile are shown in Fig. S2. Further, Raman spectroscopy was employed to study the crystallinity and estimate the number of monolayers for the $PtSe_2$ films. Figure 1 displays the Raman spectra of the pristine materials, Sb_2Se_3, $PtSe_2$, and their heterojunction. The Raman spectra of thermally crystallized Sb_2Se_3 films of various thicknesses are shown, revealing that the shapes are identical, while the ultrathin Sb_2Se_3 film exhibits the lowest intensity. Despite that

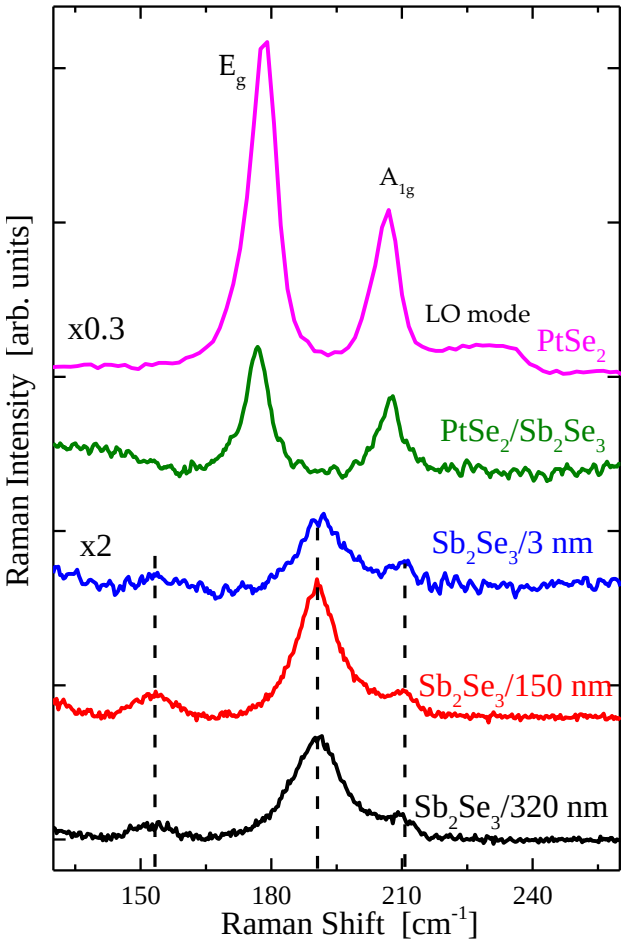

Fig. 1: Representative Raman spectra of the pristine films and the heterojunction. The top spectrum stands for the pristine $PtSe_2$ film grown on Si/SiO_2. Multiplicative factors, for better visualization of the spectra for $PtSe_2$ and ultrathin Sb_2Se_3, are applied to raw data.

a large number (30) Raman active modes are expected by the symmetry of the crystal, only a few bands are typically observed in the experimental Raman spectra. In the spectral range shown in Fig. 1, the Sb_2Se_3 spectra contain the three characteristic bands of the crystal, located at ~153 (E_g^2), ~190 (A_{1g}^2) and ~211 (combination mode) cm^{-1}, in accordance with literature results [22,23]. The absence of bands near 234 and 250 cm^{-1} demonstrates the lack of both elemental Se and oxides on the film surface, respectively, which indicates excellent stoichiometry and good purity of the Sb_2Se_3 films.

$PtSe_2$ crystals grow in the 1T octahedral structure which is characterized by the D_{3d} point group symmetry. Like any other transition metal dichalcogenide, $PtSe_2$ exhibits layer-dependent Raman spectra. The two main Raman modes with symmetries A_{1g} and E_g correspond to out-of-plane and in-plane vibration of Se atoms, respectively. Raman spectra of pure $PtSe_2$ (top spectrum) are collected by crystals grown on Si/SiO_2 substrate with pre-deposited Pt layer with minimum thickness. The E_g and A_{1g} peaks are observed at 178 and 207 cm^{-1}, respectively. Along with these two prominent vibrational peaks, a broad weak band in the area 230-235 cm^{-1} arises as the superposition of IR-active modes A_{2u} and E_u. These values agree with the literature data by O' Brien *et al.* [24] who proposed a useful correlation among Raman spectra parameters and the thickness of the $PtSe_2$ layer. The wavenumber of the E_g band and the band intensity ratio A_{1g} / E_g are useful indicators of the film thickness. For the current spectra of pristine $PtSe_2$ we find $E_g \approx 178$ cm^{-1} and $A_{1g} / E_g \approx 0.5$. Based on the data provided in Ref. [24], our spectra reveal a pristine $PtSe_2$ film thickness up to 1.5 nm. It is worth mentioning that the optical and band alignment studies for the heterojunction in this work, refer to $PtSe_2$ grown on the ultrathin Sb_2Se_3 film.

As far as the heterojunction is concerned, the vibrational modes of $PtSe_2$, which is the top layer, dominate the Raman spectra. Due to the higher Raman cross section of $PtSe_2$

in comparison to Sb_2Se_3, and the stronger absorption of the former at the laser energy (1.96 eV), the weak intensity of Raman modes of the Sb_2Se_3 film (underlayer) is not resolved in the spectrum. The E_g and A_{1g} peaks appear at 177 and 207 cm^{-1}, respectively and the A_{1g}/E_g intensity ratio is of about 0.6. These values for the heterojunction indicate a similar thickness of the $PtSe_2$ film grown on Sb_2Se_3, i.e. less than 1.5 nm. Slight changes in the band wavenumbers and the intensity ratio observed between the pristine $PtSe_2$ film on Si/SiO_2 and the heterojunction may arise from interactions of the $PtSe_2$ with the Sb_2Se_3.

Optical absorption curves were transformed to the form of Tauc plots, which can provide insight into the character of the optical absorption. The Tauc plot has emerged as a versatile method in determining optical properties of amorphous and crystalline thin films, such as the magnitude and the type (direct or indirect) of the optical bandgap E_g. In particular, the absorption coefficient, α depends on energy according to the following relations:

$$\alpha = 0 \qquad \text{for } E < E_g \qquad 1(a)$$

$$(ahv)^n = B\left(hv - E_g\right) \qquad \text{for } E > E_g \qquad 1(b)$$

where h is Planck's constant, v is the frequency of light, and B is a proportionality constant. The value of the exponent n is indicative of the type of the electronic transition, as it can be used to determine whether the transition is direct (i.e. negligible variation of the electron wave-vector), indirect, allowed or forbidden. Specifically, for direct allowed transitions $n = 2$, for direct forbidden transitions $n = 2/3$, for indirect allowed transitions $n = 1/2$ and for indirect forbidden transitions $n = 1/3$. Considering that the allowed transitions are prevailing in the absorption processes, the typical explored cases pertain to the exponents, $n = 2$ and $n = 1/2$, for the direct and indirect transition, respectively. Therefore, $(ahv)^n$ is plotted against the photon energy by

choosing the proper value of n that creates a linear dependence for a certain photon energy range. An extrapolation of the linear part of the absorption coefficient, intersects the energy axis at the value of the direct or indirect bandgap, E_g. In a more generalized approach, the absorption coefficient is described by a combination of processes involving direct and indirect transitions, represented by the first and second terms, respectively, of Eq. (2), [25]

$$\alpha h\nu = B'\left(h\nu - E_g^{dir}\right)^{1/2} + B''\left(h\nu - E_g^{ind} \mp E_{ph}\right)^2 \quad (2)$$

where B' and B'' are proportionality constants, E_{ph} is the absorbed/emitted phonon energy, and E_g^{dir}, E_g^{ind} are the direct and indirect bands energies, respectively. Neglecting reflection from the film's surface, the absorption coefficient of a film of thickness d, is calculated by the measured absorptance, $A = 1 - T - R$, (where T and R stand for the transmittance and reflectance, respectively) via the relation [26]:

$$\alpha(cm^{-1}) = \frac{1}{d} ln\left(\frac{A}{T}\right) \quad (3)$$

Despite that Sb_2Se_3 is a material which has been thoroughly studied over the last thirty years, there are still contradictory reports in the current literature about the direct [27] or indirect [28–30] nature of the optical bandgap of this semiconductor. It has been reported that the bandgap magnitude lies (typically) in the range 1.0 – 1.5 eV, while higher values (up to 1.8 eV) have also been reported. Early works on single crystals have suggested that indirect forbidden [31,32] transitions are responsible for the changes of the absorption coefficient. It has also been reported in a temperature-dependent study [27] that the bandgap is direct at low temperatures (5 – 100 K) and indirect at high temperatures (100 – 300 K). Further, representing the absorption coefficient data both with the $n = 1/2$ and $n = 2$ values, it has been shown [33] that the corresponding linear parts of each curve could provide both the indirect (1.1 eV) and direct [18,34] bandgaps of Sb_2Se_3. The Tauc plot shown in Fig. 2(a) reveals that the $n = 1/2$ transforms the

experimental data to a better straight line than the $n = 2$ exponent. Therefore, the indirect bandgap of Sb_2Se_3 is estimated to be $E_g^{ind} \approx 1.05$ eV, in agreement with the majority of the previous recent studies [30].

$PtSe_2$, a more recently explored material, exhibits a layer-dependent bandgap as is the case of other TMDCs. However, the dependence of the bandgap on the number of monolayers for $PtSe_2$, is much stronger than that observed in other typical layered dichalcogenide crystals. Bulk $PtSe_2$ exhibits semimetallic character (zero bandgap) whereas a semimetal-to-semiconductor transition takes place when the number of layers decreases below 3. The mono- and bi-layer have bandgaps of ~1.2 (direct) and ~0.2 eV, respectively [35]. A bandgap of ~0.75 for the bilayer at room temperature has also been reported [36]. Notably, there are reports about a much weaker dependence of the optical bandgap on the number of layers Zhao *et al*. [37] who estimated bandgaps ranging for 0.97 to 0.57 eV when the thickness varies in the range from 2 to 8 nm. The authors assigned this unexpected finding to the coexistence of semiconducting and semimetallic for CVD-grown $PtSe_2$ films.

Figure 2(b) shows the experimentally measured absorptance curves for pristine $PtSe_2$ and the heterojunction, $Sb_2Se_3/PtSe_2$. The curves bear the same shape as those reported elsewhere [38] over a wide energy range. Obviously, in the case of the heterojunction, the absorption of the $PtSe_2$ film dominates the absorption spectrum in relation to the absorption of Sb_2Se_3. Using Eq. (2), the indirect bandgaps of these materials were found to be $E_g^{ind}(PtSe_2) \sim 0.30 \pm 0.05$ eV and $E_g^{ind}(Sb_2Se_3/PtSe_2) \sim 0.40 \pm 0.05$ eV. The phonon energies for $PtSe_2$ is too low, ~0.02 eV, i.e. less than the error, to affect these values. Despite the discrepancies in previously reported results about the thickness-dependence of the bandgap magnitude in $PtSe_2$, as stated above, the values obtained by the current

study suggest that the $PtSe_2$ films (pristine and heterojunction) are up to 2 or 3 monolayers thick.

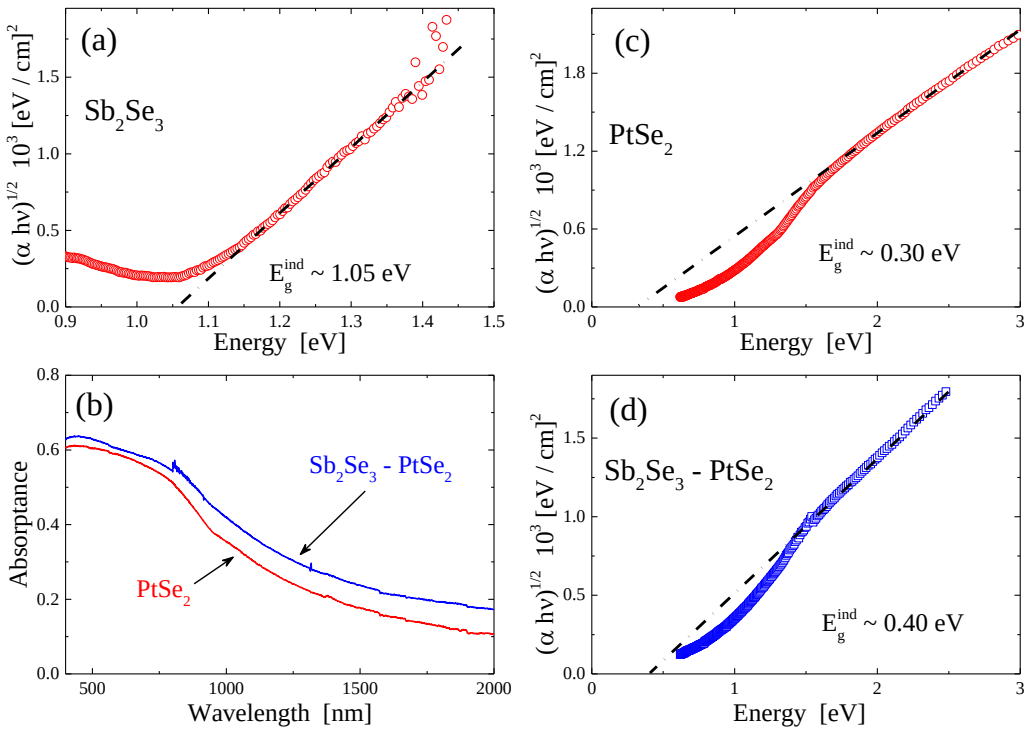

Fig. 2: (a) Tauc plot $(ahv)^{1/2}$ vs. energy for the Sb_2Se_2 pristine film. **(b)** Absorptance curves for pristine $PtSe_2$ and the Sb_2Se_3 heterojunction. **(c)** Tauc plot $(ahv)^{1/2}$ vs. energy for the $PtSe_2$ pristine film. **(d)** Tauc plot $(ahv)^{1/2}$ vs. energy for the Sb_2Se_3 / $PtSe_2$ heterojunction. The dashed lines represent best fits to the linear parts of the experimental data.

XPS and UPS have been employed to investigate the energy band alignment at $PtSe_2$ /Sb_2Se_3 heterojunction with a focus on the estimation of the valence band offset (VBO) ΔE_V, and the conduction band offset, ΔE_C. The ΔE_V can be derived based on a method by Kraut *et al.* [39], using the core level (CL) energy spectra of the related atoms, whereas ΔE_C is estimated using the energy bandgaps calculated from the Tauc plots [40]. UPS measurements, shown in Fig. S3, were performed in order to estimate the ionization potential, i.e. the energy distance between the valence band maximum (VBM) and the

vacuum level. Details are provided in the SI file. To apply the Kraut method the binding energy of the core levels and the VBM must be measured for the two neat materials and their heterojunction. The overlayer materials of the heterojunction must be thin enough to allow the penetration, through this layer, of the photoelectrons arising from the underneath film. Therefore, XPS peaks from both layers need to be resolved in a single measurement. According to the Kraut's method ΔE_V is defined as:

$$\Delta E_V = \left(E_{CL}^{PtSe_3} - E_{VBM}^{PtSe_3}\right) - \left(E_{CL}^{Sb_2Se_3} - E_{VBM}^{Sb_2Se_3}\right) + \Delta E_{CL} \quad (4a)$$

Where $E_{CL}^{PtSe_2} - E_{VBM}^{PtSe_2}$ denotes the core level BE ($Pt4f_{7/2}$) relative to the VBM of the deposited $PtSe_2$, $E_{CL}^{Sb_2Se_3} - E_{VBM}^{Sb_2Se_3}$ correspond to the core level BE ($Sb3d_{5/2}$) with respect to the VBM of the underlying Sb_2Se_3 and ΔE_{CL} represents the BE separation of two core levels from materials Sb_2Se_3 and $PtSe_2$ for the heterojunction.

The conduction band offset (CBO) ΔE_C, is calculated as:

$$\Delta E_C = E_g^{Sb_2Se_3} - E_g^{PtSe_2} - \Delta E_V. \quad (4b)$$

XPS analysis of the ultrathin Sb_2Se_3 film (~ 3 nm) reveals the presence of an oxide overlayer Sb_2O_3 as shown in Fig. 3(a) [39]. The Sb3d peak consists of two Sb3d doublets (with spin-orbit separation of 9.25 eV) due to Sb_2Se_3 and Sb_2O_3; additionally, a single O1s peak at 532.2eV is visible [14]. The oxide thickness, *d*, is determined from the XPS intensities of Sb3d components using an appropriate model, which is based on the ratio, *R*, of component's intensities of each Sb_2Se_3 and Sb_2O_3 chemical states and the attenuation experienced by the Sb3d electrons passing through the Sb_2O_3 overlayer (inelastic mean free path, λ=1.56 nm) [41,42]. In the current case, the native oxide is formed due to air exposure of the Sb_2Se_3 surface after being removed from the sputtering chamber. Therefore, the equation for the oxide thickness is simplified to $d = L\cos(\alpha)\ln(K \cdot R + 1)$, where L is the effective attenuation length, equal to ~$0.9 \times \lambda \approx$ 1.4 nm, and K is the intensity ratio of Sb_2Se_3 and Sb_2O_3 materials in their bulk form.

The above estimation yields $d \approx 1.4 \pm 0.2$ nm. The region near the valence band maximum is shown enlarged in Fig. 3a, which serves to determine VBM positions for each material. The binding energies of $Sb3d_{5/2}$ relative to valence band are: $E_{CL}^{Sb_2O_3} - E_{VBM}^{Sb_2O_3} = 530.16 \pm 0.05eV$ and $E_{CL}^{Sb_2Se_3} - E_{VBM}^{Sb_2Se_3} = 528.73 \pm 0.05eV$ for Sb_2O_3 and Sb_2Se_3, respectively.

In order to investigate the effect of the oxide on the Sb_2Se_3 surface, a reference sample was prepared by additional selenization of Sb_2Se_3 at 300 ºC for 30 min to substitute Se for O. This sample was immediately transferred to the XPS chamber to avoid surface oxidation. The XPS data of this pure Sb_2Se_3 film are presented in Fig. 3(b). The BE position of $Sb3d_{5/2}$ relative to VBM is $E_{CL}^{Sb_2Se_3} - E_{VBM}^{Sb_2Se_3} = 529.04 \pm 0.05eV$ which does not differ significantly from the Sb_2Se_3 film with the oxide overlayer. This finding demonstrates that partial oxidation does not practically affect the material electronic properties which are of interest in this study.

Figure 4(a) shows the Pt4f and the VBM of a reference $PtSe_2$ thick film. The binding energy of $Pt4f_{7/2}$ is $E_{CoreLevel}^{PtSe_2} - E_{VBM}^{PtSe_2} = 72.85 \pm 0.05eV$, in agreement to the literature value [43]. The absence of Pt-O and Pt-Pt bonds indicates the high quality of

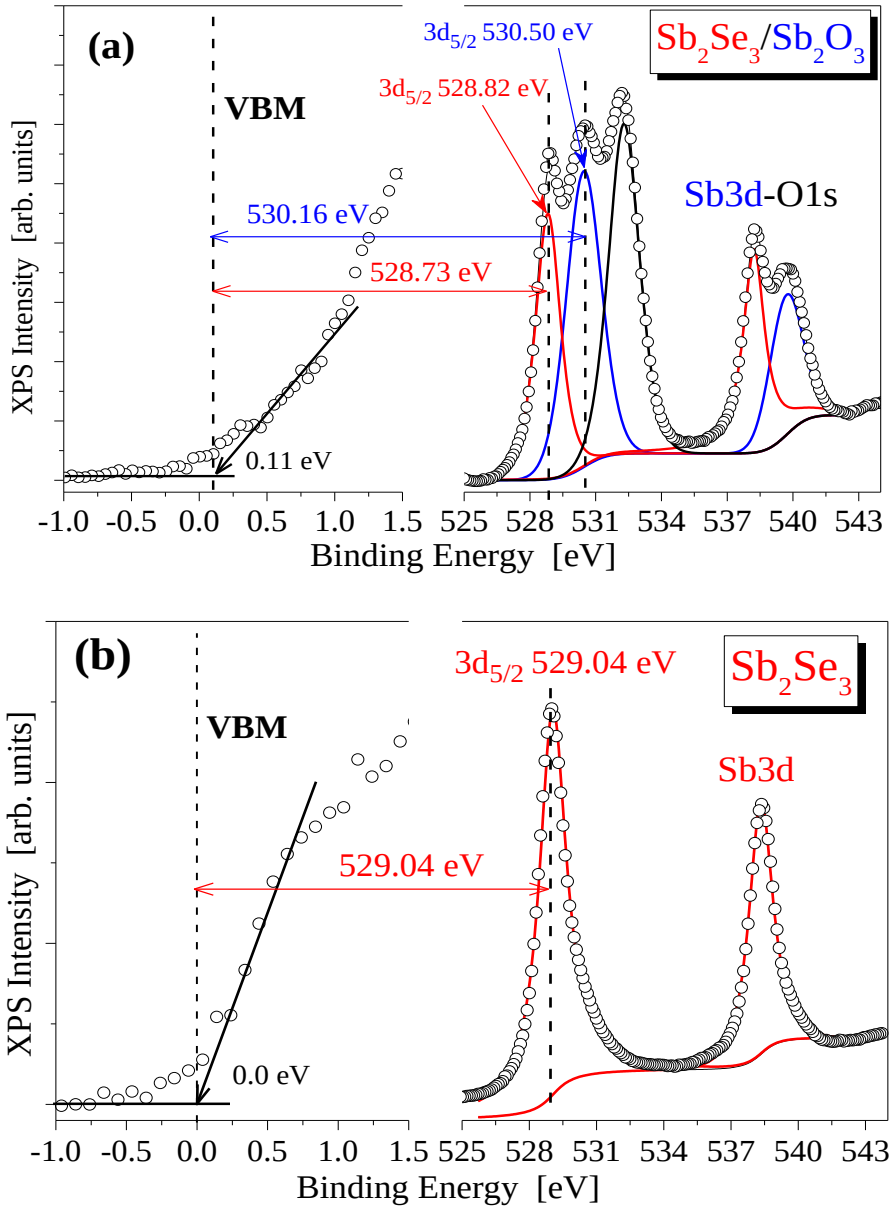

Fig. 3: Deconvoluted Sb3d peaks and valence band maximum of **(a)** an ultrathin Sb_2Se_3 film deposited on BK7, and **(b)** a freshly selenized, oxygen-free, Sb_2Se_3 film.

the $PtSe_2$ crystals. Figure 4(b) shows the Pt4f and Sb3d peaks of the ultrathin $PtSe_2$ / Sb_2Se_3 heterojunction. The Sb3d spectrum for the heterojunction is identical to the corresponding spectra of ultrathin Sb_2Se_3 sample with the oxide overlayer (shown in Fig. 3) demonstrating both components, i.e. Sb_2Se_3 and Sb_2O_3 along with O1s peak.

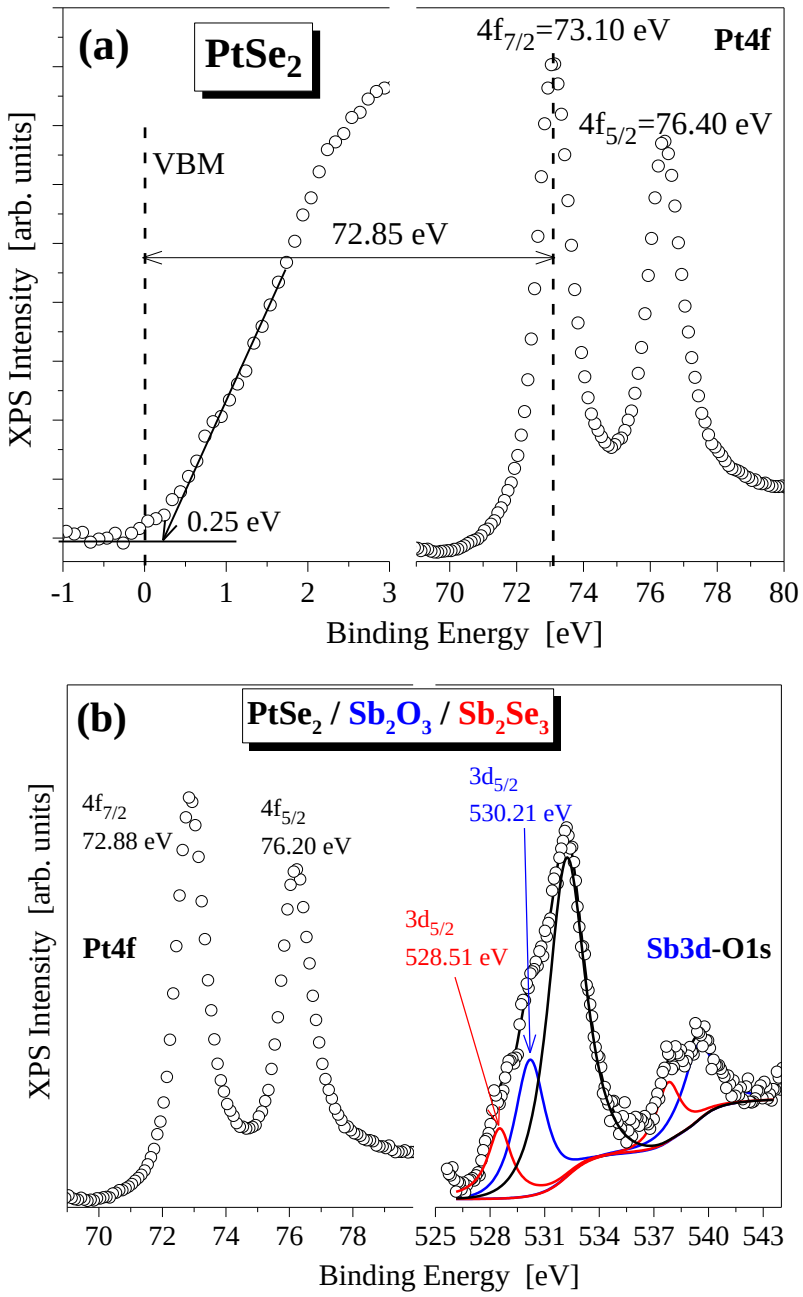

Fig. 4: (a) Pt4f peak and valence band maximum of a thick $PtSe_2$ film. **(b)** Pt4f and deconvoluted Sb3d peaks of the PtSe2 / Sb_2Se_3 heterojunction.

The $PtSe_2$ film thickness is calculated using the peak intensities of Pt4f and Sb3d considering a homogeneous $PtSe_2$ thin film and is ~2.5 nm. The binding energy difference between $Pt4f_{7/2}$ and $Sb3d_{5/2}$ (of the Sb_2Se_3 component) is $\Delta E_{CL} = 455.63 \pm 0.05eV$. Thus, the VBO between the $PtSe_2$ and Sb_2Se_3 estimated by Eq. (4a) is $\Delta E_V =$

$-0.25eV \pm 0.05eV$. Consequently, the CBO calculated via Eq. (4b) is $\Delta E_C = 1.0eV \pm 0.05eV$. Combining the XPS/UPS analysis and the optical band gaps calculated from the Tauc's plot, the energy level positions, the "natural" band alignment of the interface and the proposed band structure for the $PtSe_2$ / Sb_2Se_3 heterojunction, are illustrated in Fig. 5.

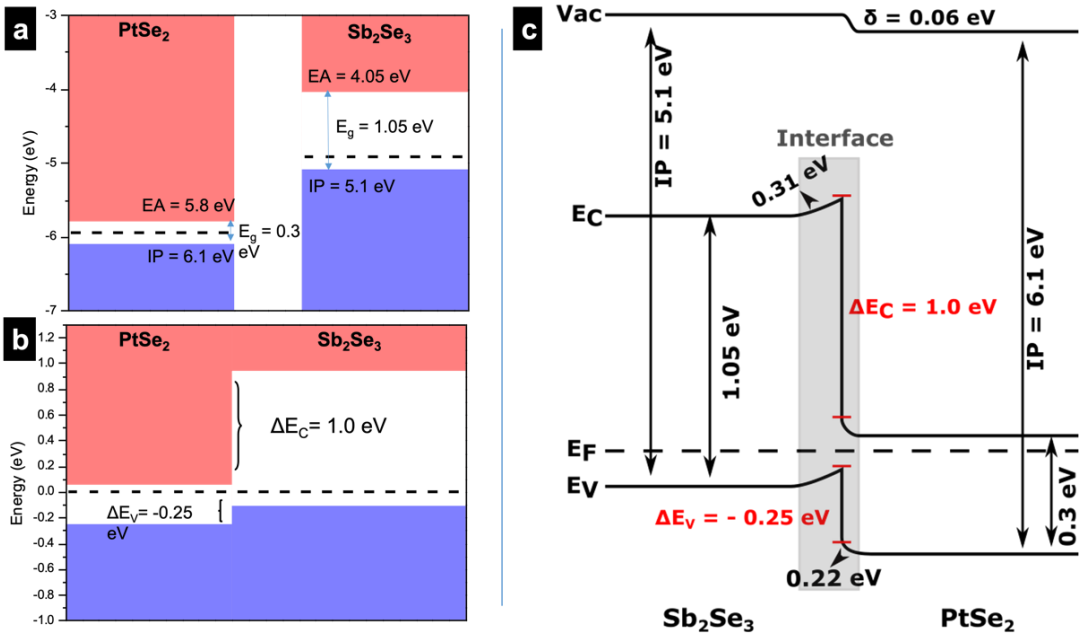

Fig. 5: (a) Energy level positions determined by XPS for $PtSe_2$ and Sb_2Se_3, showing electron affinity (EA) and ionization potential (IP) of each material. **(b)** band alignment of the interface between $PtSe_2$ and Sb_2Se_3 based on the Kraut's method. **(c)** Schematic band structure diagram for the $PtSe_2$/Sb_2Se_3 heterojunction. For clarity, the energy levels are not shown in scale.

The band structure of the interface is of great importance for the functionality of a device built with this heterojunction. The above analysis demonstrates that the $PtSe_2$/Sb_2Se_3 heterojunction exhibits band alignment of type II at the interface, exhibiting a staggered gap. It is well known, that in their majority van der Waals heterojunctions exhibit type II band alignment [44]. Such heterojunction structure implies

that after the photogeneration of charge carriers, electrons and holes move towards opposing direction through the interface, engendering a built-in electric field due to the spatial separation. Indeed, when the interface is formed, electrons will flow for the material with the higher E_F (Sb_2Se_3) to that of the lower E_F value ($PtSe_2$), which will create a built-in voltage. Such charge distribution is essential for photodetectors, photovoltaics and other optoelectronic devices, where the control over charge carriers critically affects device performance. It should be noted that an ultrathin layer of Sb_2O_3 is sandwiched between the capping layer of $PtSe_2$ and the Sb_2Se_3 underlayer film. As discussed above, this oxide layer is formed due to the exposure of as-prepared Sb_2Se_3 films to the ambient environment and the high proclivity of this material to oxidation. The presence of the oxide has been investigated in detail by Shiel *et al*. [14] who studied the band alignment of Sb_2O_3 and Sb_2Se_3. The influence of native oxides due to air exposure was compared with intentionally deposited Sb_2O_3 films. Negative valence band offset was observed for both the air-exposed and the intentionally deposited oxides. The difference in values was attributed to various factors including the polycrystalline vs. single crystal structure and the thickness of the oxide layers. On the same direction, Fleck *et al*. [45] studied the effect of oxides, grown due to air exposure, on the time-dependent performance of photovoltaic devices. Interestingly, the presence of ultrathin layers of oxide, through which holes can tunnel, results in enhanced device performance in comparison to Sb_2Se_3 samples stored in vacuum. The oxide over layer (~ 1 nm) creates Se-rich Sb_2Se_3 underlayers that in turn assist efficient performance, although thicker oxide layers can be detrimental for the devices. In this regard, our findings demonstrate that the $PtSe_2$ overlayer provides shielding preventing further oxidation. At the same time, the thin oxide layer present at the interface between $PtSe_2$

and Sb_2Se_3 is beneficial for PV devices, albeit detailed device study is necessary before drawing solid conclusions.

In such type II heterojunctions, light absorption can be extended to longer wavelengths in relation to the absorption edges of the individual components. The van der Waals epitaxy between $PtSe_2$ and Sb_2Se_3 permits the unstrained growth of one material on top of the other even if their lattice parameters do not perfectly match, as is the case of these materials, i.e. 3.98 Å (Sb_2Se_3) and 3.75 Å ($PtSe_2$). The van der Waals epitaxy of 2D materials arises from their fairly chemically inert surfaces and can significantly reduce the strict requirements for lattice matching in epitaxial growth. The lack of an appreciable fraction of dangling bonds decreases the covalent bonding of the epilayer atoms. Overall, the van der Waals epitaxy benefits from the strain-free growth and the proper rotational alignment among the two materials. It should also be emphasized that irrespective of the growth method, i.e. selenization of a Pt ultrathin film, or other growth method of the Sb_2Se_3 / $PtSe_2$ systems, the bonding characteristics of the heterojunction between two materials with "inert" outer surfaces, will be similar, because it will be ultimately dictated by the van der Waals interactions. From a device perspective, this is important because the constrain of a truly epitaxially grown interface can be lifted.

4. Conclusion

In summary, a van der Waals heterojunction of $PtSe_2/Sb_2Se_3$ was prepared in a direct way that does not necessitate the transfer of any of these materials. Ultrathin Pt films were evaporated onto Sb_2Se_3 films and were selenized at low temperature to prepare crystals of high purity and crystallinity. The heterojunction was investigated by Raman spectroscopy, optical absorption and XPS/UPS. Raman spectra revealed the successful growth of few layer (less than ~3) $PtSe_2$, which was confirmed by optical absorption,

resulting in indirect bandgaps for both the $PtSe_2$ and the $PtSe_2/Sb_2Se_3$ heterojunction, namely ~0.30±0.05 eV and ~0.40±0.05 eV, respectively. The combination of XPS and UPS data enable the construction of the band structure diagram for the $PtSe_2/Sb_2Se_3$ heterojunction interface, which was found to be of type II. Due to the particular attention paid to Sb_2Se_3 over the last years in the field of photovoltaics owing to its enhanced absorption, the fact that $PtSe_2/Sb_2Se_3$ heterojunction exhibits type-II behavior is essential. Indeed, type-II heterojunctions are currently under scrutiny because they offer enhanced charge separation between the carriers which is beneficial to develop high performance optoelectronic devices. Further, the current study has shown that the $PtSe_2$ overlayer acts as a barrier layer eliminating the oxidation of the very sensitive to ambient condition Sb_2Se_3 underlayer. The handy benefits provided by the particular heterojunction between materials of different dimensionality, i.e. 2D/$PtSe_2$ – 1D/Sb_2Se_3, may pave the way for a rational design in the field of trans-dimensional heterostructures.

Funding: K.B. and S.N.Y. acknowledge support by the European Union's H2020 research and innovation programme under the Marie Skłodowska-Curie grant agreement N. 721642 (SOLUTION).

Supporting information: FESEM morphology of heterostructure, AFM surface morphology along with height profile of ultrathin Sb_2Se_3 and Secondary Ion cut-off and valence band cut-off information derived from UPS data.

Acknowledgment: A. Chrissanthopoulos is thanked for his assistance with optical absorption experiments. We are thankful to Mrs E. Bellou and Prof. C. Galiotis for their assistance in AFM measurements.

Author contributions: K.B. and S.N.Y. conceived the idea. K.B., M.C. and D.R. prepared samples, performed experiments and analyzed the data. L.S. conducted the XPS/UPS measurements and the corresponding data analysis. S.N.Y. drafted the manuscript with input from all authors. All the authors discussed the results and commented on the manuscript.

Data availability statement: All data needed to evaluate the conclusions in the paper are present in the paper.

References:

(1) Khan, K.; Tareen, A. K.; Aslam, M.; Wang, R.; Zhang, Y.; Mahmood, A.; Ouyang, Z.; Zhang, H.; Guo, Z. Recent Developments in Emerging Two-Dimensional Materials and Their Applications. *J. Mater. Chem. C* **2020**, *8* (2), 387–440. https://doi.org/10.1039/C9TC04187G.

(2) Li, M.-Y.; Chen, C.-H.; Shi, Y.; Li, L.-J. Heterostructures Based on Two-Dimensional Layered Materials and Their Potential Applications. *Mater. Today* **2016**, *19* (6), 322–335. https://doi.org/10.1016/j.mattod.2015.11.003.

(3) Jiang, Y.; Chen, S.; Zheng, W.; Zheng, B.; Pan, A. Interlayer Exciton Formation, Relaxation, and Transport in TMD van Der Waals Heterostructures. *Light Sci. Appl.* **2021**, *10* (1), 72. https://doi.org/10.1038/s41377-021-00500-1.

(4) Front Matter. In *Chalcogenide Glasses*; Elsevier, 2014; pp i–iii. https://doi.org/10.1016/B978-0-85709-345-5.50020-9.

(5) Kostadinova, O.; Yannopoulos, S. N. Raman Spectroscopic Study of SbxSe100−x Phase-Separated Bulk Glasses. *J. Non. Cryst. Solids* **2009**, *355* (37–42), 2040–2044. https://doi.org/10.1016/j.jnoncrysol.2008.07.046.

(6) Ngo, T. T.; Chavhan, S.; Kosta, I.; Miguel, O.; Grande, H.-J.; Tena-Zaera, R. Electrodeposition of Antimony Selenide Thin Films and Application in Semiconductor Sensitized Solar Cells. *ACS Appl. Mater. Interfaces* **2014**, *6* (4), 2836–2841. https://doi.org/10.1021/am405416a.

(7) Luo, M.; Leng, M.; Liu, X.; Chen, J.; Chen, C.; Qin, S.; Tang, J. Thermal Evaporation and Characterization of Superstrate CdS/Sb 2 Se 3 Solar Cells. *Appl. Phys. Lett.* **2014**, *104* (17), 173904. https://doi.org/10.1063/1.4874878.

(8) Wilson, J. A.; Yoffe, A. D. The Transition Metal Dichalcogenides Discussion and Interpretation of the Observed Optical, Electrical and Structural Properties. *Adv. Phys.* **1969**, *18* (73), 193–335. https://doi.org/10.1080/00018736900101307.

(9) Zhou, Y.; Wang, L.; Chen, S.; Qin, S.; Liu, X.; Chen, J.; Xue, D.-J.; Luo, M.; Cao, Y.; Cheng, Y.; Sargent, E. H.; Tang, J. Thin-Film Sb2Se3 Photovoltaics with Oriented One-Dimensional Ribbons and Benign Grain Boundaries. *Nat. Photonics* **2015**, *9* (6), 409–415. https://doi.org/10.1038/nphoton.2015.78.

(10) Miró, P.; Ghorbani-Asl, M.; Heine, T. Two Dimensional Materials Beyond MoS 2 : Noble-Transition-Metal Dichalcogenides. *Angew. Chemie Int. Ed.* **2014**, *53* (11), 3015–3018. https://doi.org/10.1002/anie.201309280.

(11) Zhao, Y.; Qiao, J.; Yu, P.; Hu, Z.; Lin, Z.; Lau, S. P.; Liu, Z.; Ji, W.; Chai, Y. Extraordinarily Strong Interlayer Interaction in 2D Layered PtS 2. *Adv. Mater.* **2016**, *28* (12), 2399–2407. https://doi.org/10.1002/adma.201504572.

(12) Wang, G.; Wang, K.; McEvoy, N.; Bai, Z.; Cullen, C. P.; Murphy, C. N.; McManus, J. B.; Magan, J. J.; Smith, C. M.; Duesberg, G. S.; Kaminer, I.; Wang, J.; Blau, W. J. Ultrafast Carrier Dynamics and Bandgap Renormalization in Layered PtSe 2. *Small* **2019**, *15* (34), 1902728. https://doi.org/10.1002/smll.201902728.

(13) Wang, G.; Wang, Z.; McEvoy, N.; Fan, P.; Blau, W. J. Layered PtSe 2 for Sensing, Photonic, and (Opto-)Electronic Applications. *Adv. Mater.* **2021**, *33* (1), 2004070. https://doi.org/10.1002/adma.202004070.
(14) Shiel, H.; Hobson, T. D. C.; Hutter, O. S.; Phillips, L. J.; Smiles, M. J.; Jones, L. A. H.; Featherstone, T. J.; Swallow, J. E. N.; Thakur, P. K.; Lee, T.-L.; Major, J. D.; Durose, K.; Veal, T. D. Band Alignment of Sb 2 O 3 and Sb 2 Se 3. *J. Appl. Phys.* **2021**, *129* (23), 235301. https://doi.org/10.1063/5.0055366.
(15) Jiang, J.; Guo, Y.; Weng, X.; Long, F.; Xin, Y.; Lu, Y.; Ye, Z.; Ruan, S.; Zeng, Y.-J. A Tailorable Polarity-Flipping Response in Self-Powered, Flexible Sb_2Se_3/ZnO Bilayer Photodetectors. *J. Mater. Chem. C* **2021**, *9* (14), 4978–4988. https://doi.org/10.1039/D1TC00786F.
(16) Xin, Y.; Jiang, J.; Lu, Y.; Liang, H.; Zeng, Y.; Ye, Z. Self-Powered Broad Spectral Photodetector with Ultrahigh Responsivity and Fast Response Based on Sb 2 Se 3 /VO 2 Heterojunction. *Adv. Mater. Interfaces* **2021**, *8* (10), 2100058. https://doi.org/10.1002/admi.202100058.
(17) Chen, S.; Zheng, Z.; Cathelinaud, M.; Ma, H.; Qiao, X.; Su, Z.; Fan, P.; Liang, G.; Fan, X.; Zhang, X. Magnetron Sputtered Sb2Se3-Based Thin Films towards High Performance Quasi-Homojunction Thin Film Solar Cells. *Sol. Energy Mater. Sol. Cells* **2019**, *203*, 110154. https://doi.org/10.1016/j.solmat.2019.110154.
(18) Ren, D.; Chen, S.; Cathelinaud, M.; Liang, G.; Ma, H.; Zhang, X. Fundamental Physical Characterization of Sb 2 Se 3 -Based Quasi-Homojunction Thin Film Solar Cells. *ACS Appl. Mater. Interfaces* **2020**, *12* (27), 30572–30583. https://doi.org/10.1021/acsami.0c08180.
(19) Meyzonnette, J.-L.; Mangin, J.; Cathelinaud, M. Refractive Index of Optical Materials; 2019; pp 997–1045. https://doi.org/10.1007/978-3-319-93728-1_29.
(20) Boland, C. S.; Coileáin, C. Ó.; Wagner, S.; McManus, J. B.; Cullen, C. P.; Lemme, M. C.; Duesberg, G. S.; McEvoy, N. PtSe 2 Grown Directly on Polymer Foil for Use as a Robust Piezoresistive Sensor. *2D Mater.* **2019**, *6* (4), 045029. https://doi.org/10.1088/2053-1583/ab33a1.
(21) Yim, C.; Passi, V.; Lemme, M. C.; Duesberg, G. S.; Ó Coileáin, C.; Pallecchi, E.; Fadil, D.; McEvoy, N. Electrical Devices from Top-down Structured Platinum Diselenide Films. *npj 2D Mater. Appl.* **2018**, *2* (1), 5. https://doi.org/10.1038/s41699-018-0051-9.
(22) Bera, A.; Pal, K.; Muthu, D. V. S.; Sen, S.; Guptasarma, P.; Waghmare, U. V.; Sood, A. K. Sharp Raman Anomalies and Broken Adiabaticity at a Pressure Induced Transition from Band to Topological Insulator in Sb2Se3. *Phys. Rev. Lett.* **2013**, *110* (10), 107401. https://doi.org/10.1103/PhysRevLett.110.107401.
(23) Vidal-Fuentes, P.; Guc, M.; Alcobe, X.; Jawhari, T.; Placidi, M.; Pérez-Rodríguez, A.; Saucedo, E.; Roca, V. I. Multiwavelength Excitation Raman Scattering Study of Sb 2 Se 3 Compound: Fundamental Vibrational Properties and Secondary Phases Detection. *2D Mater.* **2019**, *6* (4), 045054. https://doi.org/10.1088/2053-1583/ab4029.
(24) O'Brien, M.; McEvoy, N.; Motta, C.; Zheng, J.-Y.; Berner, N. C.; Kotakoski, J.; Elibol, K.; Pennycook, T. J.; Meyer, J. C.; Yim, C.; Abid, M.; Hallam, T.; Donegan, J. F.; Sanvito, S.; Duesberg, G. S. Raman Characterization of Platinum Diselenide Thin Films. *2D Mater.* **2016**, *3* (2), 021004. https://doi.org/10.1088/2053-1583/3/2/021004.
(25) Optical Properties of Solids. In *A Modern Course in the Quantum Theory of Solids*; WORLD SCIENTIFIC, 2012; pp 499–579. https://doi.org/10.1142/9789814417150_0008.
(26) Ritter, D.; Weiser, K. Suppression of Interference Fringes in Absorption Measurements on Thin Films. *Opt. Commun.* **1986**, *57* (5), 336–338. https://doi.org/10.1016/0030-4018(86)90270-1.
(27) Chen, C.; Li, W.; Zhou, Y.; Chen, C.; Luo, M.; Liu, X.; Zeng, K.; Yang, B.; Zhang, C.; Han, J.; Tang, J. Optical Properties of Amorphous and Polycrystalline Sb 2 Se 3 Thin Films Prepared by Thermal Evaporation. *Appl. Phys. Lett.* **2015**, *107* (4), 043905.

https://doi.org/10.1063/1.4927741.
(28) Rodríguez-Lazcano, Y.; Peña, Y.; Nair, M. T. S.; Nair, P. K. Polycrystalline Thin Films of Antimony Selenide via Chemical Bath Deposition and Post Deposition Treatments. *Thin Solid Films* **2005**, *493* (1–2), 77–82. https://doi.org/10.1016/j.tsf.2005.07.238.
(29) Gilbert, L. R.; Van Pelt, B.; Wood, C. The Thermal Activation Energy of Crystalline Sb2Se3. *J. Phys. Chem. Solids* **1974**, *35* (12), 1629–1632. https://doi.org/10.1016/S0022-3697(74)80175-7.
(30) Chen, C.; Bobela, D. C.; Yang, Y.; Lu, S.; Zeng, K.; Ge, C.; Yang, B.; Gao, L.; Zhao, Y.; Beard, M. C.; Tang, J. Characterization of Basic Physical Properties of Sb2Se3 and Its Relevance for Photovoltaics. *Front. Optoelectron.* **2017**, *10* (1), 18–30. https://doi.org/10.1007/s12200-017-0702-z.
(31) Kosek, F.; Tulka, J.; Štourač, L. Optical, Photoelectric and Electric Properties of Single-Crystalline Sb2Se3. *Czechoslov. J. Phys.* **1978**, *28* (3), 325–330. https://doi.org/10.1007/BF01597220.
(32) Birkett, M.; Linhart, W. M.; Stoner, J.; Phillips, L. J.; Durose, K.; Alaria, J.; Major, J. D.; Kudrawiec, R.; Veal, T. D. Band Gap Temperature-Dependence of Close-Space Sublimation Grown Sb 2 Se 3 by Photo-Reflectance. *APL Mater.* **2018**, *6* (8), 084901. https://doi.org/10.1063/1.5027157.
(33) El-Shair, H.; Ibrahim, A.; Abd El-Wahabb, E.; Afify, M.; Abd El-Salam, F. Optical Properties of Sb2Se3 Thin Films. *Vacuum* **1991**, *42* (14), 911–914. https://doi.org/10.1016/0042-207X(91)90557-Y.
(34) Ren, D.; Luo, X.; Chen, S.; Zheng, Z.; Cathelinaud, M.; Liang, G.; Ma, H.; Qiao, X.; Fan, X.; Zhang, X. Structure, Morphology, and Photoelectric Performances of Te-Sb2Se3 Thin Film Prepared via Magnetron Sputtering. *Nanomaterials* **2020**, *10* (7), 1358. https://doi.org/10.3390/nano10071358.
(35) Wang, Y.; Li, L.; Yao, W.; Song, S.; Sun, J. T.; Pan, J.; Ren, X.; Li, C.; Okunishi, E.; Wang, Y.-Q.; Wang, E.; Shao, Y.; Zhang, Y. Y.; Yang, H.; Schwier, E. F.; Iwasawa, H.; Shimada, K.; Taniguchi, M.; Cheng, Z.; Zhou, S.; Du, S.; Pennycook, S. J.; Pantelides, S. T.; Gao, H.-J. Monolayer PtSe 2 , a New Semiconducting Transition-Metal-Dichalcogenide, Epitaxially Grown by Direct Selenization of Pt. *Nano Lett.* **2015**, *15* (6), 4013–4018. https://doi.org/10.1021/acs.nanolett.5b00964.
(36) Gulo, D. P.; Yeh, H.; Chang, W.-H.; Liu, H.-L. Temperature-Dependent Optical and Vibrational Properties of PtSe2 Thin Films. *Sci. Rep.* **2020**, *10* (1), 19003. https://doi.org/10.1038/s41598-020-76036-y.
(37) Zhao, X.; Liu, F.; Liu, D.; Yan, X.-Q.; Huo, C.; Hui, W.; Xie, J.; Ye, Q.; Guo, C.; Yao, Y.; Liu, Z.-B.; Tian, J.-G. Thickness-Dependent Ultrafast Nonlinear Absorption Properties of PtSe 2 Films with Both Semiconducting and Semimetallic Phases. *Appl. Phys. Lett.* **2019**, *115* (26), 263102. https://doi.org/10.1063/1.5135375.
(38) Yim, C.; McEvoy, N.; Riazimehr, S.; Schneider, D. S.; Gity, F.; Monaghan, S.; Hurley, P. K.; Lemme, M. C.; Duesberg, G. S. Wide Spectral Photoresponse of Layered Platinum Diselenide-Based Photodiodes. *Nano Lett.* **2018**, *18* (3), 1794–1800. https://doi.org/10.1021/acs.nanolett.7b05000.
(39) Kraut, E. A.; Grant, R. W.; Waldrop, J. R.; Kowalczyk, S. P. Precise Determination of the Valence-Band Edge in X-Ray Photoemission Spectra: Application to Measurement of Semiconductor Interface Potentials. *Phys. Rev. Lett.* **1980**, *44* (24), 1620–1623. https://doi.org/10.1103/PhysRevLett.44.1620.
(40) Shiel, H.; Hutter, O. S.; Phillips, L. J.; Swallow, J. E. N.; Jones, L. A. H.; Featherstone, T. J.; Smiles, M. J.; Thakur, P. K.; Lee, T.-L.; Dhanak, V. R.; Major, J. D.; Veal, T. D. Natural Band Alignments and Band Offsets of Sb 2 Se 3 Solar Cells. *ACS Appl. Energy Mater.* **2020**, *3* (12), 11617–11626. https://doi.org/10.1021/acsaem.0c01477.
(41) Jablonski, A.; Zemek, J. Overlayer Thickness Determination by XPS Using the Multiline Approach. *Surf. Interface Anal.* **2009**, *41* (3), 193–204.

https://doi.org/10.1002/sia.3005.
(42) Sygellou, L.; Ladas, S.; Reading, M. A.; van den Berg, J. A.; Conard, T.; De Gendt, S. A Comparative X-Ray Photoelectron Spectroscopy and Medium-Energy Ion-Scattering Study of Ultra-Thin, Hf-Based High-k Films. *Surf. Interface Anal.* **2010**, *42* (6–7), 1057–1060. https://doi.org/10.1002/sia.3251.
(43) Jiang, W.; Wang, X.; Chen, Y.; Wu, G.; Ba, K.; Xuan, N.; Sun, Y.; Gong, P.; Bao, J.; Shen, H.; Lin, T.; Meng, X.; Wang, J.; Sun, Z. Large-area High Quality PtSe 2 Thin Film with Versatile Polarity. *InfoMat* **2019**, inf2.12013. https://doi.org/10.1002/inf2.12013.
(44) Zheng, Z.; Zu, X.; Zhang, Y.; Zhou, W. Rational Design of Type-II Nano-Heterojunctions for Nanoscale Optoelectronics. *Mater. Today Phys.* **2020**, *15*, 100262. https://doi.org/10.1016/j.mtphys.2020.100262.
(45) Fleck, N.; Hutter, O. S.; Phillips, L. J.; Shiel, H.; Hobson, T. D. C.; Dhanak, V. R.; Veal, T. D.; Jäckel, F.; Durose, K.; Major, J. D. How Oxygen Exposure Improves the Back Contact and Performance of Antimony Selenide Solar Cells. *ACS Appl. Mater. Interfaces* **2020**, *12* (47), 52595–52602. https://doi.org/10.1021/acsami.0c14256.

TOC-

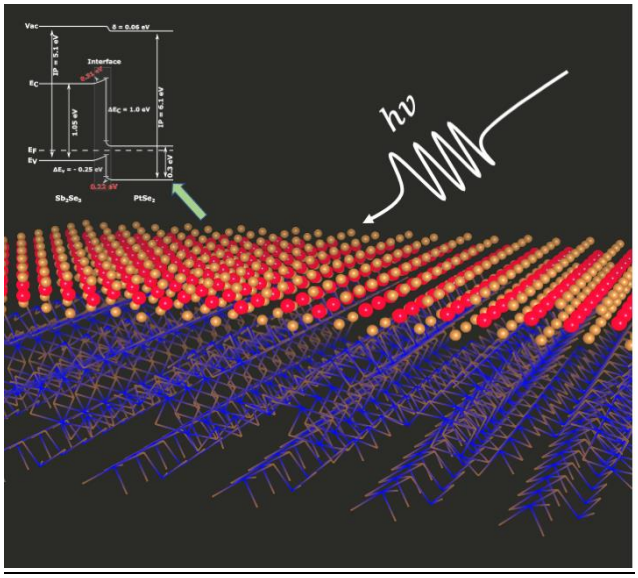

Supporting Information

Band alignment and optical properties of 1D/2D $Sb_2Se_3/PtSe_2$ heterojunctions

Kapil Bhorkar,[a,b,*,] Labrini Sygellou,[a] Michel Cathelinaud,[b] Donglou Ren[b], Jean-Luc Adam,[b] and

Spyros N. Yannopoulos [a,*]

[a] *Foundation for Research and Technology Hellas – Institute of Chemical Engineering Sciences (FORTH/ICE-HT), P.O. Box 1414, GR-26504, Rio-Patras, Greece*

[b] *Univ Rennes, CNRS, ISCR - UMR 6226, F-35000 Rennes, France*

*Email: sny@iceht.forth.gr, kapilbhorkar@gmail.com

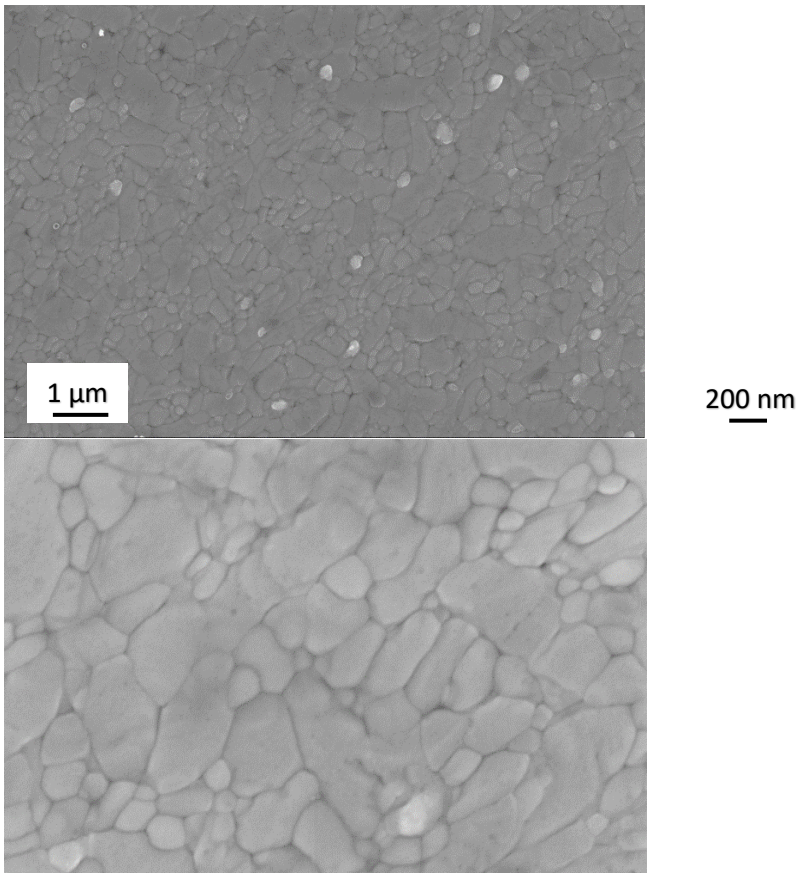

Figure S1: FE-SEM images of $Sb_2Se_3/PtSe_2$ heterostructure surface demonstrating polycrystalline morphology.

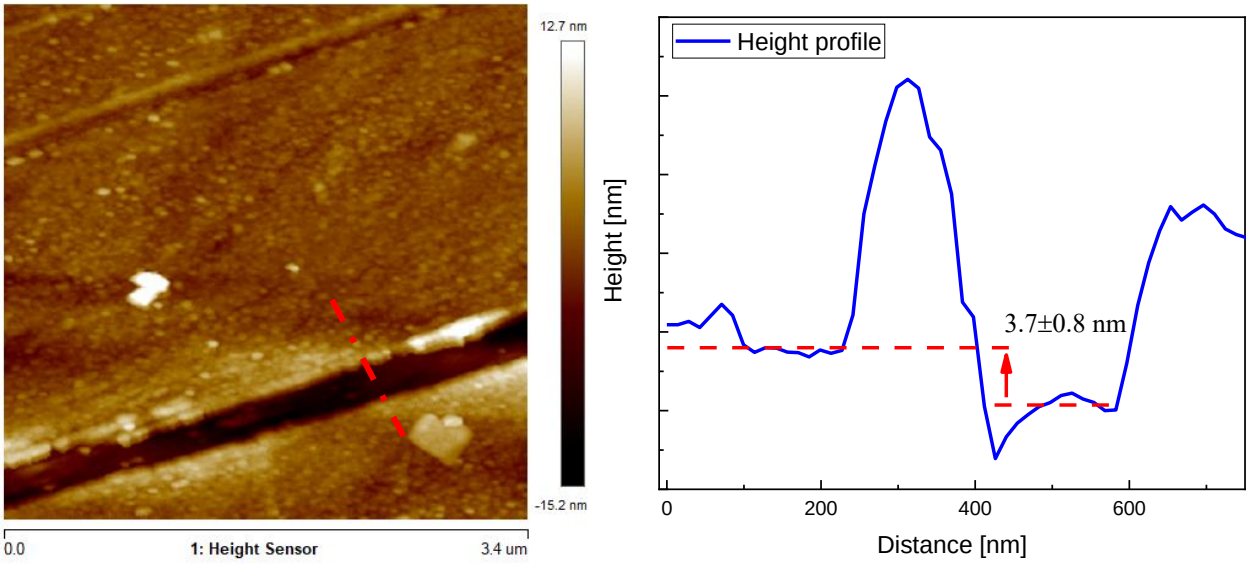

Surface roughness ~ 1.86nm

Figure S2: AFM image of Sb_2Se_3 on silica surface demonstrating polycrystalline morphology and height thickness of ~3.7 nm with surface roughness of approximately 1.86 nm.

All AFM measurements were performed on a Bruker Dimension Icon under ambient conditions. PeakForce-Quantitative nano-Mechanical (PF-QnM): Silicon nitride ScanAsyst-Air probe (R=2 nm, k=0.4 N/m, f=70 kHz) was used for topographic images. The forces exerted were as low as possible in order to get a better visualization of the finer sample features.

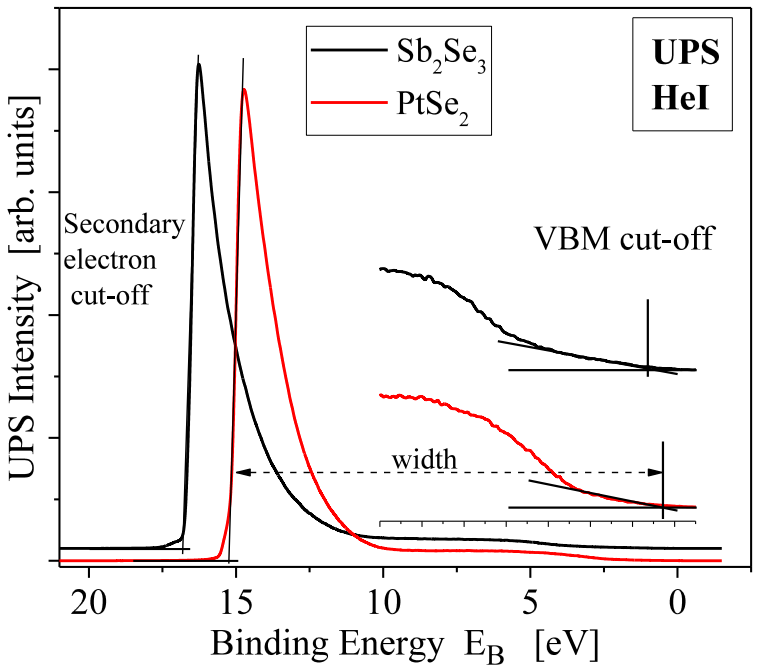

Figure S3: UPS spectra for neat Sb_2Se_3 (black line) and $PtSe_2$ (red line) samples. The low binding energy region is shown enlarged.

UPS spectra of neat Sb_2Se_3 and $PtSe_2$ films. The ionization potential is determined by subtracting the spectral width from the HeI excitation energy, $h\nu$ = 21.22 eV. The spectral

width, is derived by linear extrapolation of the secondary electron cut-off and the valence band maximum cut-off as shown in the figure. According to this estimation: IP (Sb_2Se_3) = hv – width = 21.22 - (16.74 - 0.65) = 5.13 ± 0.05 eV and IP ($PtSe_2$) = hv – width = 21.22 - (15.34 - 0.26) = 6.16 ± 0.05 eV.